PHYSICS

Sound vortex diffraction via topological charge in phase gradient metagratings

Yangyang Fu[1]*[†], Chen Shen[2]*, Xiaohui Zhu[2]*, Junfei Li[2], Youwen Liu[1], Steven A. Cummer[2†], Yadong Xu[3†]

Wave fields with orbital angular momentum (OAM) have been widely investigated in metasurfaces. By engineering acoustic metasurfaces with phase gradient elements, phase twisting is commonly used to obtain acoustic OAM. However, it has limited ability to manipulate sound vortices, and a more powerful mechanism for sound vortex manipulation is strongly desired. Here, we propose the diffraction mechanism to manipulate sound vortices in a cylindrical waveguide with phase gradient metagratings (PGMs). A sound vortex diffraction law is theoretically revealed based on the generalized conservation principle of topological charge. This diffraction law can explain and predict the complicated diffraction phenomena of sound vortices, as confirmed by numerical simulations. To exemplify our findings, we designed and experimentally verified a PGM based on Helmholtz resonators that support asymmetric transmission of sound vortices. Our work provides previously unidentified opportunities for manipulating sound vortices, which can advance more versatile design for OAM-based devices.

INTRODUCTION

Vortices are common phenomena in fluid dynamics, such as whirlpools, smoke rings, and tornados. Inspired by hydrodynamic vortices, the concept of optical vortices was proposed by Coullet *et al.* (*1*) in 1989 by revealing the vortex solutions of the Maxwell-Bloch equations. Later, Allen *et al.* (*2*) found that optical vortices can carry orbital angular momentum (OAM), which is characterized by a helical wavefront, i.e., $\exp(il\theta)$, where the integer l is known as topological charge and θ is the azimuthal angle. Distinct from the two available states in spin angular momentum of light, defined by the chirality of circularly polarized light, the number of allowable OAM states of light is unbounded. Owing to the fascinating properties of OAM, optical vortices have been widely studied in the past decades (*3*). In particular, metasurfaces (*4*), i.e., artificial structures with subwavelength thickness, have provided a powerful platform for OAM-based applications (*5*, *6*). Examples include OAM generation (*4*, *7*), OAM multiplexing and demultiplexing (*8*, *9*), and spin to OAM conversion (*10*).

In contrast to light waves, acoustic waves only carry OAM, as acoustic waves are essentially scalar pressure fields and generally considered spinless (*11*, *12*). Acoustic OAM has recently drawn notable attention, and several OAM-based applications were proposed, such as particle manipulation (*13*, *14*) and acoustic torque (*15*, *16*). To generate acoustic OAM, people have proposed active and passive methods. The active method is generally implemented by large active transducer arrays (*17–19*), which require conversions between acoustic and electronic signals as well as relatively complicated feedback circuitry. On the other hand, the passive approach uses compact and low-cost structures that can convert a uniform wavefront into a spiral shape wavefront or sound vortex (SV) by designing thickness-gradient structures (*20*, *21*), spiral arms

(*22*, *23*), and acoustic metasurfaces (*24–27*). These approaches can be directly understood from the conversion principle of topological charge as we summarize below in Eq. 3, where l^{ξ} is the topological charge provided from gradient structures. For example, acoustic OAM of $l^t = 1$ (*24*, *25*) was produced from incident uniform wavefront with $l^{in} = 0$ and acoustic metasurface with $l^{\xi} = 1$.

To date, the generation and manipulation mechanisms of acoustic OAM are mainly based on the twisting phase (*20–27*) or the geometric phase effect (*28*, *29*). The former has limited abilities in manipulating SVs, as the designed transmission (reflection) structure only provides a single transmitted (reflected) channel. SV manipulation in the latter relies on the coupling between OAM and helical structures, and its bulk geometry design hinders practical applications. A more powerful mechanism for manipulating SVs is strongly desired to expand the capabilities of current OAM-based devices. Recent advances in planar metasurfaces (*30–33*) have shown that multiple reflections therein can induce more versatile diffraction phenomena. Inspired by that work, we propose here the diffraction mechanism to manipulate SVs in a three-dimensional (3D) cylindrical waveguide with phase gradient metagratings (PGMs), which are also called gradient index metasurfaces (*34–37*). The proposed metastructure harnesses the grating effects and combines both grating and gradient elements by design, which distinguishes it from previous work where the metalayer solely acts as a simple phase twist device (*25*, *26*). We find that SV diffraction can be realized via artificial topological charge from PGMs, which has not been previously reported in either optics or acoustics, to the best of our knowledge. Moreover, the generalized conservation principle of topological charge is proposed to reveal theoretically the diffraction law of SVs, which can explain and predict the complicated diffraction phenomena of SVs. We find that, depending on a critical topological charge (l^c), incident SVs take different diffraction orders. For topological charge within l^c, the incident vortex is directly converted as the transmitted vortex by taking the lowest order, while for topological charge beyond l^c, the incident vortex can take either the transmitted channel or the reflected channel of higher diffraction order, which depends on the integer parity (i.e., oddness or evenness) of the propagation number of multiple reflections (i.e., the number of times the wave

[1]College of Science, Nanjing University of Aeronautics and Astronautics, Nanjing 211106, China. [2]Department of Electrical and Computer Engineering, Duke University, Durham, NC 27708, USA. [3]School of Physical Science and Technology, Soochow University, Suzhou 215006, China.
*These authors contributed equally to this work.
†Corresponding author. Email: yyfu@nuaa.edu.cn (Y.F.); cummer@duke.edu (S.A.C.); ydxu@suda.edu.cn (Y.X.)

travels inside the PGM). The propagation number is relevant to the diffraction order and the number of unit cells of PGM, and the integer parity of multiple reflections could be controlled by odd/even design for unit cells of PGM. Therefore, benefitting from the multiple reflection effect in PGMs, SV diffraction in our proposed system is powerful and versatile and delivers more possibilities for vortex manipulation even compared with optical vortex diffraction in grating systems (7–9). For example, on the basis of the diffraction law, asymmetric transmission of SVs is exploited as a new OAM-based device. A PGM using Helmholtz resonators is designed and fabricated, and asymmetric transmission of SVs is observed in experiments. Furthermore, a unidirectional, multichannel OAM-based communication device is demonstrated. Our work reveals a general material-mediated conversion rule for SVs, which will drive more research on acoustic OAM and boost applications in acoustic communication.

RESULTS

Models and theory

Let us consider a PGM in a cylindrical waveguide of radius R filled with air as shown in Fig. 1A, where the PGM with thickness of h consists of l^ξ groups of fanlike supercells (see Fig. 1B). Each supercell has an angular width of $\vartheta = 2\pi/l^\xi$ and is composed of m groups of fanlike unit cells with angular width of $\vartheta_1 = \vartheta/m$ (see Fig. 1B). The unit cells, made of sound-hard materials (see the gray regions

in Fig. 1B), are perforated by fanlike slits with angular width of ϑ_2 ($\vartheta_2 < \vartheta_1$). To achieve azimuthal phase gradient, the phase shift distribution $\phi_j(\theta)$ over each supercell should cover a range of 2π, which can be satisfied by filling m individual impedance-matched materials in the slits with different refractive indices (see the gradient color regions in Fig. 1B), i.e., $n_j = \rho_j = 1 + (j - 1)\lambda/(mh)$, where $j = 1,2\cdots m$. Hence, the phase difference of two adjacent unit cells per period is $\Delta\phi = 2\pi/m$. Note that these sound-hard materials are impenetrable for airborne acoustics; they could be designed with suitable thickness or ultrathin thickness (i.e., surface) to avoid guided wave coupling across the interior boundary of adjacent unit cells. As the PGM is equipped with l^ξ groups of supercells whose azimuthal phase distribution covers 2π, it can provide an effective topological charge of l^ξ with a clockwise helicity (see the yellow circle with arrows in Fig. 1A). Because the azimuthal phase distribution is periodically repeated for the vortex beams, the proposed PGM could be regarded as azimuthal metagrating.

For the cylindrical waveguide with a fixed radius, there only exist a finite number of vortex modes, with the number of modes depending on the working frequency or wavelength (see black dashed line in Fig. 1C), and their topological charge belongs to $[-l^M, +l^M]$, where l^M marks the maximum order of vortex modes and "+" ("−") defines clockwise (counterclockwise) helicity of propagating vortex. Considering an incident SV with topological charge of $l = l^{in}$, its acoustic field is expressed as
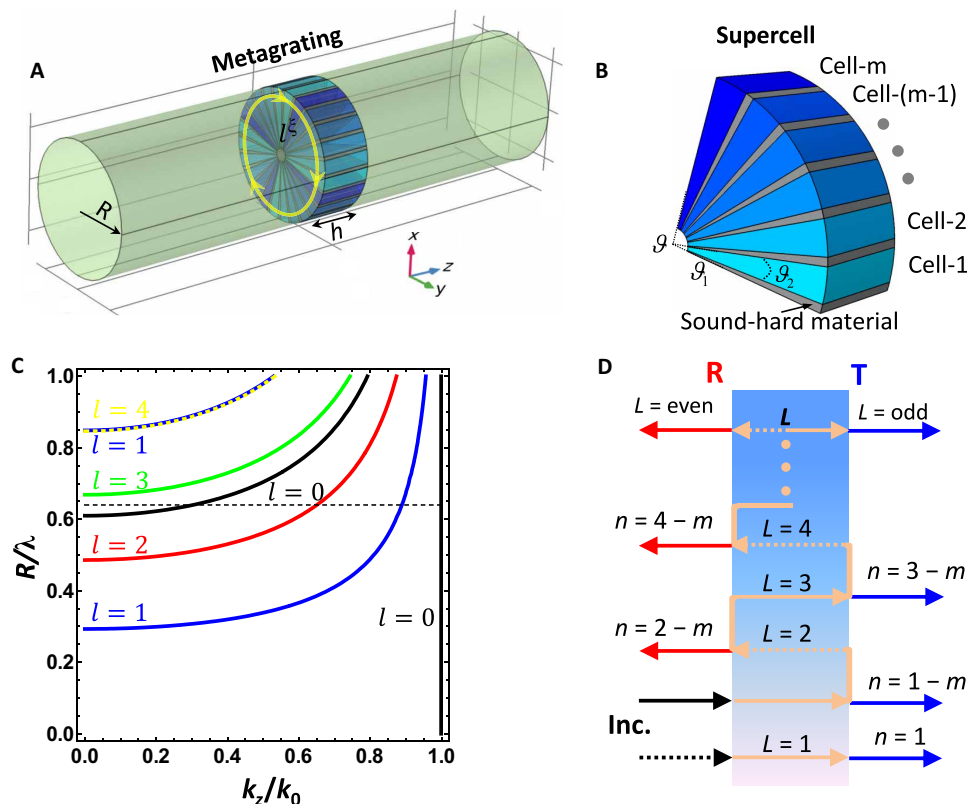

Fig. 1. Diffraction mechanism of SVs in a 3D cylindrical waveguide with PGM. (**A**) Schematic diagram of a 3D cylindrical waveguide with a PGM, which is composed of l^ξ fanlike supercells. (**B**) Topography of the fanlike supercell consisting of m groups of fanlike unit cells. These unit cells with gradient indices can produce a discrete phase modulation to cover a complete range of 2π. (**C**) Dispersion relationship of propagating vortex modes in a cylindrical waveguide, where there are two propagating modes of $l = 0$ ($l = 1$) taking values of $v = 0$ and $v = 1$ ($v = 1$ and $v = 2$), respectively, corresponding to the lower and upper curves, and the dashed line is $R = 0.64\lambda$. (**D**) Sketch map of SV diffraction in PGM.

$$p^{in} = J_l(k_{l,\nu} r)/J_l(k_{l,\nu} R)\exp(il\theta + ik_z z) \qquad (1)$$

where $\partial J_{l,\nu}(k_{l,\nu} r)/\partial(k_{l,\nu} r)\,|_{\,r=R} = 0$, $k_{l,\nu}^2 + k_z^2 = k_0^2$, $k_{l,\nu}$, and k_z are the transverse and longitudinal wave numbers, respectively; $k_0 = 2\pi/\lambda$ is the wave number in air; and $1/J_l(k_{l,\nu} R)$ is a normalized factor. According to the diffraction law of planar gratings (38, 39), the incident and reflected/transmitted vortices at reflected/transmitted interface should obey the conservation principle of topological charge in a generalized way by including the additional topological charge from PGM, i.e.

$$l^{r(t)} = l^{in} + nl^{\xi} \qquad (2)$$

where $l^{r(t)}$ is the topological charge of the reflected (transmitted) vortex and n is the diffraction order. Equation 2 could also be understood from angular momentum selection rule by operating specific $C_{l^{\xi}}$ rotation symmetry. Similar to the critical angle in the generalized Snell law (4), there is a critical topological charge for PGM in a cylindrical waveguide, which is defined as $l^c = l^M - l^{\xi}$. For the incident SV with its topological charge within the critical one (i.e., $l^{in} \in [-l^M, l^c]$), it will pass through the PGM and can be directly twisted by the PGM, with its topological charge converted as

$$l^t = l^{in} + l^{\xi} \qquad (3)$$

which corresponds to the $n = 1$ order in Eq. 2. However, for the incident SV with its topological charge beyond the critical one ($l^{in} > l^c$), the SV cannot directly pass through the PGM, as the wave vector along the z direction becomes imaginary, caused by the converted topological charge beyond the maximum order ($l^t > l^M$). As a result, multiple reflections will occur inside the metagrating, with the propagation number of waves traveling inside unit cells defined as L (see the orange lines in Fig. 1D). If waves undergo L single trips between reflected and transmitted interfaces, then the phase difference of adjacent unit cells per period is $\Delta\phi = (2\pi/m)L$. When the scattered SV takes the n-th diffraction order, the equivalent topological charge provided from the metagrating is nl^{ξ}, leading to an equivalent phase difference of $\Delta\varphi_n = (2\pi/m)n$ between adjacent unit cells per period. If these two phase differences ($\Delta\phi$ and $\Delta\varphi_n$) can match with each other, implying that when guided waves inside the unit cells oscillate back and forth with the propagation number of L, then the incident SV will take the n-th diffraction order to depart from the metagrating. As the effective diffraction order belongs to $n \le 0$ for $l^{in} > l^c$ and $L > 0$, it seems that it is impossible to achieve $\Delta\phi = \Delta\varphi_n$. However, if phase folding of 2π is applied in $\Delta\phi$, then the phase matching relationship is built as $\Delta\phi - 2\pi q = \Delta\varphi_n$ (q is positive integer), that is

$$L = qm + n \qquad (4)$$

In subwavelength metagrating systems, a phase folding of 2π ($q = 1$) is enough to achieve the phase matching condition, i.e., $L = m + n$. When L is an odd number (see the orange solid lines in Fig. 1D), it will be a transmitted SV taking the n-th diffraction order, while when L is an even number (see the orange dashed lines in Fig. 1D), it will be a reflected SV taking the n-th diffraction order. By connecting Eqs. 2 and 4, the diffraction law of SVs is further given as

$$\begin{cases} l^t = l^{in} + nl^{\xi}, & L = \text{odd} \\ -l^r = l^{in} + nl^{\xi}, & L = \text{even} \end{cases} \qquad (5)$$

As the reflected and transmitted SVs of higher diffraction order have mirror symmetry, i.e., the helicity of the reflected SV has an opposite sign with that of the transmitted one, the "−" sign is added in the formula of "l^r."

On the basis of the above diffraction law, one can predict the diffraction phenomena of SVs in a cylindrical waveguide with PGM. For an incident SV with its topological charge within the critical one, one-pass process happens in the metagrating, and then the incident SV is converted as the transmitted SV taking the lowest order of $n = 1$, which is independent of m. While for the topological charge beyond the critical one, multiple reflections will occur inside the PGM (see orange arrows in Fig. 1D). When an odd (even) propagation route of waves traveling inside the metagrating reaches diffraction condition, strong transmitted (reflected) SV can be generated by obeying Eq. 5, as schematically shown in Fig. 1D. In some cases, although several diffraction orders are simultaneously available for an incident SV to follow, the multiple reflection effect in PGM happens in sequence (see orange arrows in Fig. 1D), and the maximum diffraction order, corresponding to the minimum propagation number, is preferential to reach the diffraction condition, referring to $L = m + n$. Furthermore, if a PGM is designed by odd and even unit cells, owing to the parity transition of the propagation number, then scattering reversal effect (i.e., transmission and reflection reversal) of SVs can happen in higher-order diffraction.

Numerical demonstration for the diffraction law of sound vortices

To confirm the validity of the above theoretical formulas, numerical simulations are performed to demonstrate the scattering behaviors of SVs in a cylindrical waveguide with PGM. The radius of the waveguide is chosen as $R = 0.64\lambda$, and the maximum propagation order of SVs in such a waveguide is $l^M = 2$ (see Fig. 1C). Two supercells ($l^{\xi} = 2$) are designed for PGM, and the critical topological charge is $l^c = 0$. If each supercell is composed of five unit cells ($m = 5$), then the scattering phenomena for incident SVs with different OAM ($l^{in} \in [-2, 2]$) could be predicted from the revealed diffraction law summarized in Eqs. 3 to 5. For incident SVs with $l^{in} \in [-2, l^c]$, they will be transmitted SVs obeying Eq. 3. As we can see from Fig. 2 (A and B), the incident SVs with $l^{in} = -2$ and $l^{in} = -1$ are converted into transmitted beams with $l^t = 0$ and $l^t = 1$, respectively. In particular, for the case of $l^{in} = -2$, two different kinds of planar wavefronts are seen on the transmitted side, because two monopole modes ($l = 0$) with $l^t = 0$ are concurrently excited by observing the dispersion relationship in Fig. 1C, where two $l = 0$ modes with different wave vectors can exist at the working wavelength (see the dashed line). While for incident SVs with $l^{in} \in (l^c, 2]$, the diffraction behavior becomes complicated. For the case of $l^{in} = 1$, the maximum diffraction order is $n = -1$, accordingly, the propagation number is an even integer, $L = m + n = 4$. As a result, there should be a reflected SV with $l^r = 1$ following the lower formula of Eq. 5, as demonstrated by the numerical simulation in Fig. 2C. For the case of $l^{in} = 2$, the maximum diffraction order turns into $n = -2$, and the propagation number becomes an odd integer of $L = 3$. Accordingly, it is a transmitted SV with $l^t = -2$ following the upper formula of Eq. 5, which is numerically demonstrated in Fig. 2D.

However, if each supercell is composed of six unit cells ($m = 6$), following the diffraction law, then incident SVs with $l^{in} \in [-2, l^c]$ undergo similar transmission effects with these in the case of $m = 5$, as demonstrated by the simulated results in Fig. 2 (E and F), while

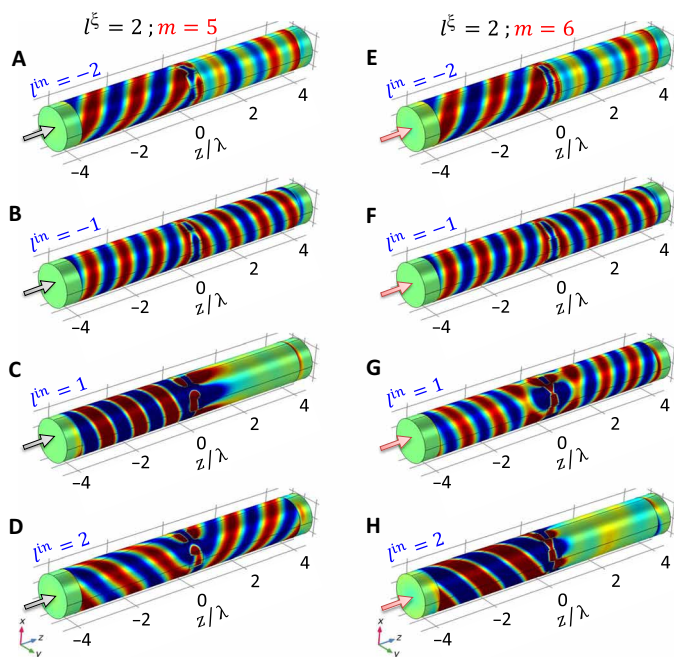**Fig. 2. Numerical demonstration for SV diffraction through ideal PGMs.** (**A** to **D**) The simulated total acoustic pressure field patterns for incident SVs with different topological charge through the PGM with $l^\xi = 2$ and $m = 5$. (**E** to **H**) The simulated total acoustic pressure field patterns for incident SVs with different topological charge through the PGM with $l^\xi = 2$ and $m = 6$. In all cases, $\vartheta_2 = 0.9\vartheta_1$, $R = 0.64\lambda$, $h = 0.5\lambda$, and $\lambda = 10$ cm. In addition, a cylinder with $0.05R$ is inserted in the center of PGMs for the convenience of simulations.

for incident SVs with $l^{in} = 1$ and $l^{in} = 2$, transmission and reflection of SVs taking higher diffraction orders will be completely reversed owing to the parity change of L. For example, for the case of $l^{in} = 1$ (see Fig. 2G), there is a transmitted SV with $l^t = -1$, which is caused by an odd propagation number of $L = m + n = 5$, while for the case of $l^{in} = 2$, the corresponding propagation number is $L = 4$, which turns into a reflected SV with $l^r = 2$ (Fig. 2H). The corresponding results of SV diffraction in Fig. 2 could be clearly observed from their phase distributions on a cross section in the transmitted/reflected area, as shown in fig. S1. Therefore, the revealed diffraction law is well confirmed by the simulated results of the PGMs with $l^\xi = 2$. In addition, the PGMs with three supercells ($l^\xi = 3$) are used to further confirm the diffraction law, shown in figs. S2 and S3. On the basis of the diffraction law of SVs, we can find that several diffraction orders could be excited for incident SVs, and therefore, PGMs can be served as multichannel OAM convertors including reflected and transmitted channels, overcoming the limit of single channel of twisting phase.

By carefully observing the above results of the PGM with $m = 5$, incident SVs with $l^{in} = \pm 1$ undergo different scattering process, that is, one can pass through the PGM with an OAM of $l^t = 1$ (see Fig. 2B), and the other one is almost reflected back with $l^r = 1$ (see Fig. 2C). Therefore, the OAM splitter can be realized for the vortex beams with $l^{in} = \pm 1$ incident from one side. If the SV with $l^{in} = -1$ or $l^{in} = 1$ is incident from the left and right sides, asymmetric transmission of SVs could be obtained in the waveguide. For example, when SV with $l^{in} = -1$ is incident from the left side of the waveguide, higher transmission of transmitted vortex with $l^t = 1$ can happen,

while for SV with $l^{in} = -1$ incident from the right side, which is identical with the case of SV with $l^{in} = 1$ incident from the left side, it will be reflected back, leading to lower transmission of the vortex beam with $l^t = -1$. In the following, practical design of the PGM and experimental measurements are performed to demonstrate the asymmetric transmission of SVs. The results not only experimentally verify our revealed diffraction law but also practically realize a new type of OAM-based device.

Practical design of PGM

To further demonstrate the diffraction law of SVs in a cylindrical waveguide with PGMs, we use Helmholtz resonators to design the above PGM with $l^\xi = 2$ and $m = 5$ at the wavelength of $\lambda = 10$ cm. Five different fanlike resonators are designed to construct the supercell of the PGM as shown in Fig. 3A, where each resonator is implemented by rotating its azimuthal section (right side) along the z axis with $\vartheta_1 = 36°$. The azimuthal section is constituted by four rows of subresonators (see the red dashed frame in Fig. 3A), and each subresonator consists of four identical Helmholtz resonators and a straight pipe (*40*). Such a four-row design can effectively enhance hybrid resonances to obtain a high transmission. Each subresonator has a height of $w = R/4 = 1.6$ cm, and the thickness of walls is $t = 1.5$ mm. To overcome the wave coupling between these fanlike resonators, five rectangular blocks with size of $h \times R \times t$ are placed behind each resonator. The transmission and phase profiles of the subresonator are displayed in Fig. 3B, in which the width of each cavity's neck is $w_{neck} = 1.5$ mm. We can see that by changing the height of cavities (w_0/w), the subresonator can cover a complete phase range of 2π with transmission coefficient beyond 90%. Five different heights of cavities are selected for these five Helmholtz resonators to obtain the required phase shifts, as marked by the yellow symbols in Fig. 3B. The fourth resonator has a slightly lower transmission (91%) than that of the other ones (more than 95%). By modifying the cavity size of the fourth resonator, given as $w_{neck} = 1.1$ mm and $w_0 = 6.33$ mm, its transmission is improved to 95.3%, yet with its phase shift unchanged. Consequently, five phase gradient resonators are designed with their transmissions all beyond 95%. Figure 3, C and D, respectively, shows the simulated acoustic field patterns of SV with $l^{in} = -1$ incident on the designed PGM from the left side and the right side of the waveguide, and the proposed asymmetric transmission of SVs is well presented in the designed PGM-based waveguide system, which are consistent with the ideal results in Fig. 2 (B and C). Tiny undesired scattering is observed in the designed results, which may be caused by the deviation of transmission and phase between the subresonator and the fanlike resonator, as the PGM is designed from 2D approximation. Better results might be achieved by directly designing individual fanlike resonators in each row and considering the change of cross section in a 3D manner (*25*). The simulated results of other SVs incident on the designed PGM are also consistent with these in the ideal cases, as shown in fig. S5. In addition, we also design the PGM with $l^\xi = 2$ and $m = 6$ (see fig. S4), and similar results fitting with the ideal cases are achieved, which are displayed in fig. S5.

Experimental demonstration for asymmetric transmission of sound vortices

Using 3D printing technology, the designed PGM is fabricated as shown in Fig. 4A. Measurements are performed in an 80-cm-long cylindrical waveguide ($R = 6.4$ cm) to verify the proposed asymmetric
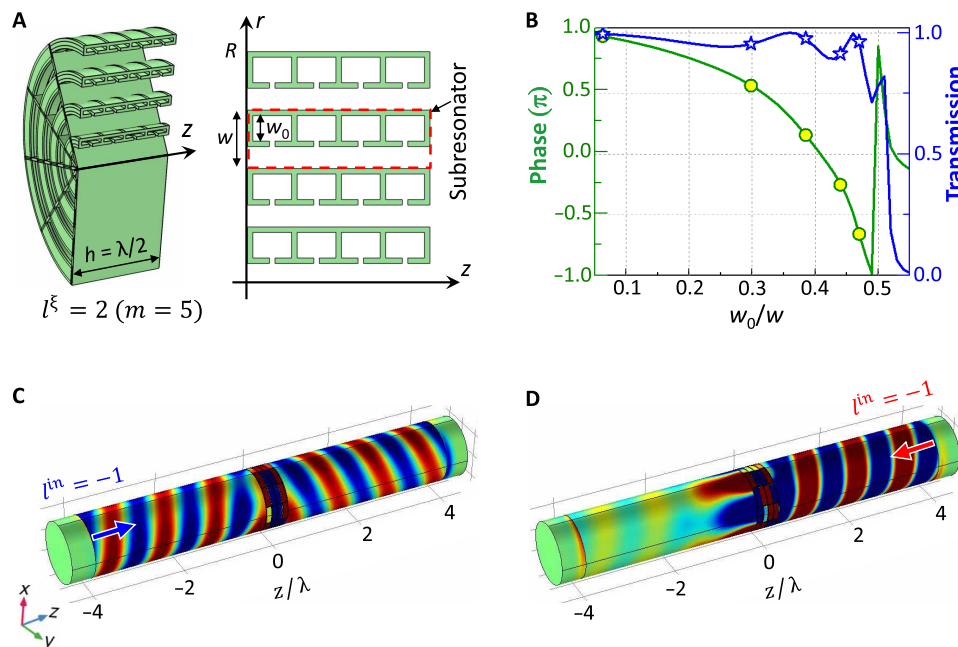
Fig. 3. Practical design for PGM. (**A**) Schematic of one supercell (left side) of the designed PGM ($l^\xi = 2$) with five ($m = 5$) different fanlike resonators at $\lambda = 10$ cm, where each resonator is realized by rotating its azimuthal section (right side) along the z axis with $\vartheta_1 = 36°$. The azimuthal section consists of four rows of four identical subresonators with height of $w = R/4 = 1.6$ cm, and the thickness of walls is $t = 1.5$ mm. Five rectangular blocks with $h \times R \times t$ are placed behind each resonator. (**B**) Transmission and phase shift versus the height ratio (w_0/w) of the 2D subresonator, in which the neck of the Helmholtz cavity is 1.5 mm. (**C**) and (**D**) are the simulated acoustic total field patterns of SV with $l^{in} = -1$ incident on the designed PGM from the left side and the right side of the waveguide, respectively.

transmission of SVs, with the sample placed in the center (see Fig. 4B). In experiments, the incident SV with $l^{in} = -1$ is generated by four mini speakers with gradient phase modulations, given as 0, $\pi/2$, π, and $3\pi/2$ (see Fig. 4B). These four speakers are arranged on a circle of radius $r_s = 0.7R$ (see Fig. 4B). The experimentally measured incident SV is shown in fig. S6, where it well agrees with the numerical result. For the SV with $l^{in} = -1$ incident from the left side (see the vortex beam with blue color in Fig. 4B), the numerically simulated phase and amplitude distributions at $z = 2.6\lambda$ (see the blue dashed curve in Fig. 4B) are displayed in Fig. 4C, where higher transmission is seen and SV with $l^t = 1$ is clearly found from the phase distribution. The experimentally measured phase and amplitude distributions are shown in the right panels of Fig. 4C, which reveal consistent results with those from numerical simulations. Because the transmission of the designed Helmholtz resonators has a slight variation in amplitude, the transmitted SV with $l^t = 1$ exhibits nonuniform transmission over the azimuth. However, the null pressure amplitudes at the center are clearly seen, exhibiting typical feature of vortex beams. For SV with $l^{in} = -1$ emitting from the right side of the waveguide (see the vortex beam with red color in Fig. 4B), the corresponding numerical and experimental results are shown in Fig. 4D. Both simulated and measured results show lower transmission of SV. The discrepancy of the phase profile in the experiment is attributed to the low transmission of SV with $l^t = -1$, as the total acoustic field can be substantially affected by other transmitted vortex modes, which are mainly composed of SV with $l^t = 1$ due to the imperfect phase and amplitude profiles of the PGM caused by fabrication errors and intrinsic losses. Moreover, the imperfect boundary conditions may also lead to a compromised result. To quantify the asymmetric transmission of SVs, transmission efficiency, defined as square root of the transmitted to incident sound power ratio is employed (25). The transmission efficiencies for the left and right incidences are numerically (experimentally) calculated as 97.6 and 16.6% (76.8 and 32.6%), respectively. The mismatch of numerical and experimental results is mainly caused by the intrinsic losses in Helmholtz resonators. By numerically introducing losses in the air channels of Helmholtz resonators [given as $\rho = 1.21$ kg/m^3 and $c = 343(1 + \gamma i)$ with $\gamma = 0.015$] to mimic the viscous and thermal dissipation, the corresponding transmission efficiencies are numerically obtained as 75.1 and 24.3%, respectively, which are consistent with the experimental results. Nevertheless, highly asymmetric transmission of SVs via the designed PGM is demonstrated in both simulations and experiments.

Unidirectional OAM-based communication

Based on of the asymmetric transmission of SVs in Fig. 4, unidirectional OAM-based communication could be further exploited as a new OAM-based device. For demonstration, two designed PGMs ($l^\xi = 2$ and $m = 5$) with a distance of 20 cm are considered in the waveguide, yet with opposite rotation direction, i.e., they have topological charge of $l^\xi = 2$ and $l^\xi = -2$ for SV propagating along the $+z$ direction (see Fig. 5A). Four active sources with gradient phase modulations are used to generate OAM information, as shown in Fig. 4B. When they are placed at the left (right) port, SV with $l^{in} = -1$ ($l^{in} = 1$) will emit from the left (right) side of the waveguide. For the case of OAM information (SV with $l^{in} = -1$) input from the left side (see Fig. 5A), it is well captured at the output side as shown in Fig. 5C. The output phase information is the same with that of the input one, although they have some deviation in amplitude due to intrinsic losses in PGMs. While for the SV with $l^{in} = 1$ incident from
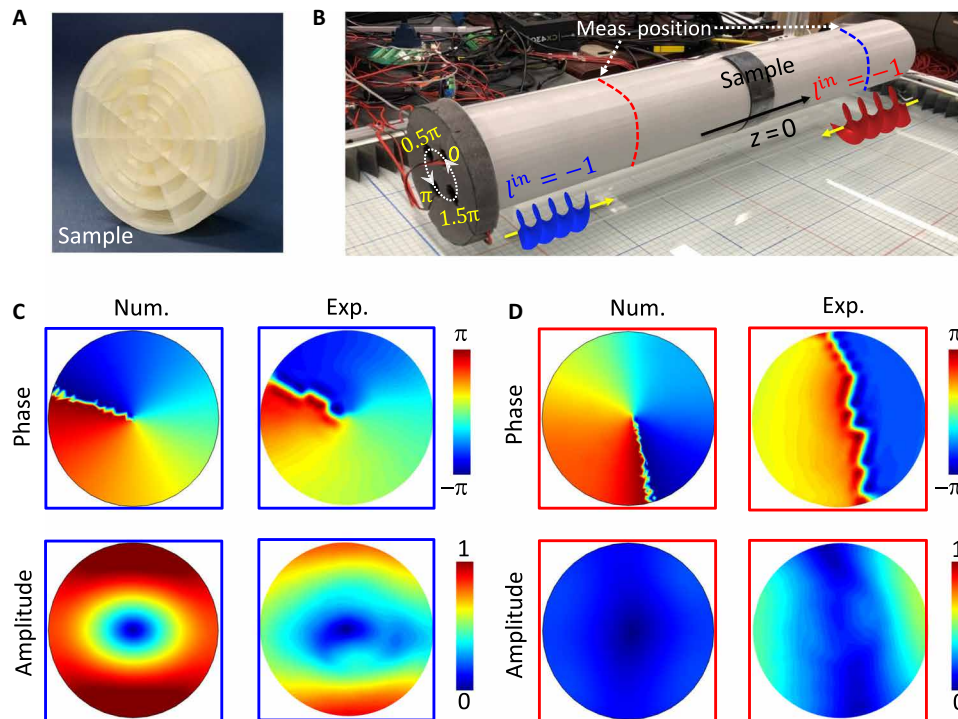
Fig. 4. Experimental demonstration for asymmetric transmission of SVs. (**A**) Fabricated sample. (**B**) Experimental setup. (**C**) Simulated (left) and measured (right) phase and amplitude distributions at $z = 2.6\lambda$ for SV with $l^{in} = -1$ incident from the left side of the waveguide. (**D**) Simulated (left) and measured (right) phase and amplitude distributions at $z = -2.6\lambda$ for SV with $l^{in} = -1$ incident from the right side of the waveguide. Photo Credit: Yangyang Fu, Nanjing University of Aeronautics and Astronautics.

the right side (see Fig. 5B), the input OAM information is greatly lost at the output side, as seen in Fig. 5D. Therefore, unidirectional OAM-based communication is well observed in the proposed PGM-based waveguide system, as information is only preserved from one direction. In the current case, only one OAM channel ($l = 1$) is used to achieve unidirectional OAM-based communication, and it could be extended to multichannel response by carefully choosing available l^M and l^ξ to design a PGM-based waveguide system. For example, on the basis of the results in fig. S2, unidirectional OAM-based multiplex communication can be realized to work in two different channels ($l = 1$ and $l = 2$) as shown in fig. S7, where two PGMs with $l^\xi = 3$ and $m = 5$ are introduced in a waveguide with $l^M = 2$. Alternatively, unidirectional OAM-based communication could also be achieved in a waveguide with multiple PGMs with $l^\xi = 1$, where incident OAM states are, respectively, retrieved from a nonzero intensity of the $l = 0$ mode at corresponding core positions based on the way of phase twisting (*26*). As shown in fig. S8, the nonzero intensities at corresponding core positions for these SVs from the left port are available to get the information of input OAM states with a single microphone, while they are null intensities for these SVs from the right port and fail to retrieve input OAM states, as also expected from the diffraction law of SVs.

DISCUSSION
In conclusion, by considering the metastructure (PGM) as azimuthal grating and introducing the generalized conservation principle of topological charge, we have proposed and revealed the diffraction

mechanism of SVs in a cylindrical waveguide, which can fully explain and predict the scattering behavior of SVs. We find that, depending on a critical topological charge, incident SVs can either transmit through PGM with the lowest diffraction order or take higher diffraction orders with the transmission and reflection depending on the integer parity of PGMs. Therefore, SV diffraction via PGMs provides versatile propagation channels, breaking through the limit of a single channel of twisting phase. Two PGMs ($l^\xi = 2$) with five and six unit cells are used to numerically demonstrate our findings. In particular, asymmetric transmission of SVs is found in the PGM ($l^\xi = 2$) with five unit cells, where the transmitted SVs with highly asymmetric amplitudes are preserved with the identical topological charge. Furthermore, we designed and fabricated the PGM ($l^\xi = 2$) with five unit cells, and asymmetric transmission of SVs is clearly observed in experiments. On the basis of the asymmetric transmission of SVs, unidirectional OAM-based communication is further demonstrated in the PGM-based waveguide system, which opens up a new away of OAM-based communication.

When the number of unit cells in a lossy PGM is increased, the transmission/reflection efficiency of the scattered SV via higher diffraction order will gradually decrease, as more propagation length via the multiple reflection effect happens in the lossy PGMs, which leads to more absorption. For example, when the SV with $l^{in} = 1$ is incident on the PGM-based waveguide (see Fig. 2C), the reflection efficiency of $l^r = 1$ greatly reduces with the increase in the number of unit cells, as shown in fig. S9A, and therefore, PGMs with simplified design (*41, 42*) can be used to reduce the undesired absorption. While for the SV with $l^{in} = -1$, the transmitted SV via the lower diffraction
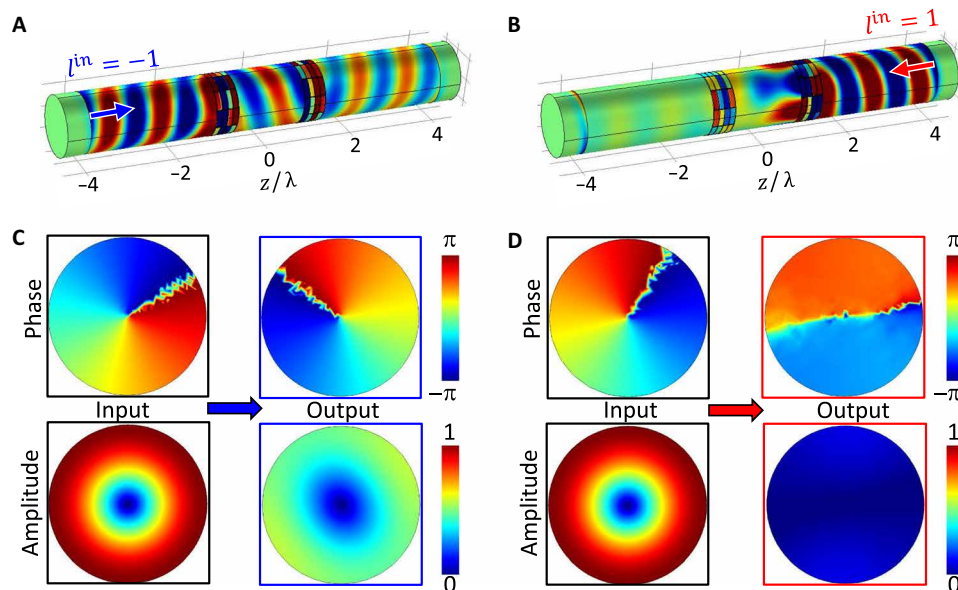
Fig. 5. Unidirectional OAM-based communication in PGM-based waveguide system. (**A**) and (**B**) are the simulated total pressure field patterns for SV with $l^{in} = -1$ and SV with $l^{in} = 1$ incident from the left and right sides, respectively. (**C**) and (**D**) are input and output phase and amplitude, corresponding to (A) and (B), respectively. In simulations, the viscous and thermal dissipation in Helmholtz resonators is mimicked by including losses in the air channels, given as $\rho = 1.21$ kg/m^3 and $c = 343(1 + \gamma i)$ with $\gamma = 0.015$. Two designed PGMs with opposite rotation direction are placed with a distance of 20 cm, and the output phase and amplitude are evaluated at planes of $z = \pm 3\lambda$.

order (i.e., Eq. 3) is almost not affected, as it undergoes one-path propagation process independent of the number of unit cells in PGMs, as shown in fig. S9B. Therefore, some potential OAM-based applications could be realized in the lossy PGM-based waveguide system, such as asymmetric OAM absorption and OAM-selected absorption. In addition, when incident SV and scattered SV have a larger wave vector, similar to diffraction properties of planar acoustic metasurfaces (*43*, *44*), undesirable/parasitic diffraction orders can appear, which might lead to a low conversion efficiency. The design strategies that incorporate bianisotropy (*27*, *45*) could be potentially used to overcome this problem. In short, the proposed diffraction law of SVs provides a clear blueprint for manipulating SVs with azimuthal phase gradient and also enables a deep understanding of the fundamental diffraction behavior in PGM-based systems and the intrinsic link between diffraction phenomena in 2D free space and 3D cylindrical waveguides. The proposed diffraction mechanism provides a new paradigm for controlling acoustic OAM and enables versatile manipulation of SVs, which can lead to numerous acoustic OAM-based applications, such as multichannel OAM convertor, OAM splitter, unidirectional transmission of OAM, and OAM-based information communication.

MATERIALS AND METHODS
Numerical simulations
The full-wave simulations are performed using COMSOL Multiphysics pressure acoustics module, where background pressure filed is used to generate SVs using the expression in Eq. 1. For simulations in Figs. 2, 3, and 5, the PGM materials are set with $\rho = 1180$ kg/m^3 and $c = 2700$ m/s, and perfectly matched layers are used in the left and right sides to reduce undesired reflections. In Fig. 4, the simulated amplitudes and phases are extracted from Fig. 3.

Experiments
The sample was fabricated with fused deposition modeling using 3D printing, and the printed material is acrylonitrile butadiene styrene plastic with density of 1180 kg/m^3 and speed of sound 2700 m/s. The fabricated PGM is placed in a cylindrical waveguide for the measurement. Four mini speakers with 0.9-cm radius are arranged on a circle of radius $r_s = 0.7R$ and are modulated with gradient input phase profiles, given as 0, $\pi/2$, π, and $3\pi/2$, to generate SV with $l^{in} = -1$. The transmitted field is scanned using a moving microphone with a step of 2.0 cm. The acoustic field at each spot is then calculated using Fourier transform. The overall scanned area is the cross section at $z = \pm 2.6\lambda$ of the waveguide, and the signal at each position is averaged out of four measurements to reduce noise. The transmitted field of empty waveguide at $z = \pm 2.6\lambda$ is also measured for normalization.

SUPPLEMENTARY MATERIALS
Supplementary material for this article is available at http://advances.sciencemag.org/cgi/content/full/6/40/eaba9876/DC1

REFERENCES AND NOTES
1. P. Coullet, L. Gil, F. Rocca, Optical vortices. *Opt. Commun.* **73**, 403–408 (1989).
2. L. Allen, M. W. Beijersbergen, R. J. C. Spreeuw, J. P. Woerdman, Orbital angular momentum of light and the transformation of Laguerre-Gaussian laser modes. *Phys. Rev. A* **45**, 8185–8189 (1992).
3. Y. Shen, X. Wang, Z. Xie, C. Min, X. Fu, Q. Liu, M. Gong, X. Yuan, Optical vortices 30 years on: OAM manipulation from topological charge to multiple singularities. *Light Sci. Appl.* **8**, 90 (2019).
4. N. Yu, P. Genevet, M. A. Kats, F. Aieta, J.-P. Tetienne, F. Capasso, Z. Gaburro, Light propagation with phase discontinuities: Generalized laws of reflection and refraction. *Science* **334**, 333–337 (2011).
5. X. Wang, Z. Nie, Y. Liang, J. Wang, T. Li, B. Jia, Recent advances on optical vortex generation. *Nanophotonics* **7**, 1533–1556 (2018).
6. M. L. N. Chen, L. J. Jiang, W. E. Sha, Orbital angular momentum generation and detection by geometric-phase based metasurfaces. *Appl. Sci.* **8**, 362 (2018).

7. K. Huang, H. Liu, S. Restuccia, M. Q. Mehmood, S.-T. Mei, D. Giovannini, A. Danner, M. J. Padgett, J.-H. Teng, C.-W. Qiu, Spiniform phase-encoded metagratings entangling arbitrary rational-order orbital angular momentum. *Light Sci. Appl.* **7**, 17156 (2018).

8. T. Lei, M. Zhang, Y. Li, P. Jia, G. N. Liu, X. Xu, Z. Li, C. Min, J. Lin, C. Yu, H. Niu, X. Yuan, Massive individual orbital angular momentum channels for multiplexing enabled by Dammann gratings. *Light Sci. Appl.* **4**, e257 (2015).

9. Y. Li, X. Li, L. Chen, M. Pu, J. Jin, M. Hong, X. Luo, Orbital angular momentum multiplexing and demultiplexing by a single metasurface. *Adv. Opt. Mater.* **5**, 1600502 (2017).

10. R. C. Devlin, A. Ambrosio, N. A. Rubin, J. P. Balthasar Mueller, F. Capasso, Arbitrary spin-to–orbital angular momentum conversion of light. *Science* **358**, 896–901 (2017).

11. K. Y. Bliokh, F. Nori, Spin and orbital angular momenta of acoustic beams. *Phys. Rev. B* **99**, 174310 (2019).

12. C. Shi, R. Zhao, Y. Long, S. Yang, Y. Wang, H. Chen, J. Ren, X. Zhang, Observation of acoustic spin. *Natl. Sci. Rev.* **6**, 707–712 (2019).

13. C. R. P. Courtney, C. E. M. Demore, H. Wu, A. Grinenko, P. D. Wilcox, S. Cochran, B. W. Drinkwater, Independent trapping and manipulation of microparticles using dexterous acoustic tweezers. *Appl. Phys. Lett.* **104**, 154103 (2014).

14. T. Wang, M. Ke, W. Li, Q. Yang, C. Qiu, Z. Liu, Particle manipulation with acoustic vortex beam induced by a brass plate with spiral shape structure. *Appl. Phys. Lett.* **109**, 123506 (2016).

15. K. Volke-Sepúlveda, A. O. Santillán, R. R. Boullosa, Transfer of angular momentum to matter from acoustical vortices in free space. *Phys. Rev. Lett.* **100**, 024302 (2008).

16. Z. Y. Hong, J. Zhang, B. W. Drinkwater, Observation of orbital angular momentum transfer from Bessel-shaped acoustic vortices to diphasic liquid-microparticle mixtures. *Phys. Rev. Lett.* **114**, 214301 (2015).

17. R. Marchiano, J.-L. Thomas, Synthesis and analysis of linear and nonlinear acoustical vortices. *Phys. Rev. E* **71**, 066616 (2005).

18. A. Riaud, J.-L. Thomas, E. Charron, A. Bussonnière, O. B. Matar, M. Baudoin, Anisotropic swirling surface acoustic waves from inverse filtering for on-chip generation of acoustic vortices. *Phys. Rev. Appl.* **4**, 034004 (2015).

19. C. Shi, M. Dubois, Y. Wang, X. Zhang, High-speed acoustic communication by multiplexing orbital angular momentum. *Proc. Natl. Acad. Sci. U.S.A.* **114**, 7250–7253 (2017).

20. J. L. Ealo, J. C. Prieto, F. Seco, Airborne ultrasonic vortex generation using flexible ferroelectrets. *IEEE Trans. Ultrason. Ferroelectr. Freq. Control* **58**, 1651–1657 (2011).

21. R. Wunenburger, J. I. V. Lozano, E. Brasselet, Acoustic orbital angular momentum transfer to matter by chiral scattering. *New J. Phys.* **17**, 103022 (2015).

22. X. Jiang, J. Zhao, S.-l. Liu, B. Liang, X.-y. Zou, J. Yang, C.-W. Qiu, J.-c. Cheng, Broadband and stable acoustic vortex emitter with multi-arm coiling slits. *Appl. Phys. Lett.* **108**, 203501 (2016).

23. N. Jiménez, V. Romero-García, L. M. García-Raffi, F. Camarena, K. Staliunas, Sharp acoustic vortex focusing by Fresnel-spiral zone plates. *Appl. Phys. Lett.* **112**, 204101 (2018).

24. L. Ye, C. Qiu, J. Lu, K. Tang, H. Jia, M. Ke, S. Peng, Z. Liu, Making sound vortices by metasurfaces. *AIP Adv.* **6**, 085007 (2016).

25. X. Jiang, Y. Li, B. Liang, J.-C. Cheng, L. Zhang, Convert acoustic resonances to orbital angular momentum. *Phys. Rev. Lett.* **117**, 034301 (2016).

26. X. Jiang, B. Liang, J.-C. Cheng, C.-W. Qiu, Twisted acoustics: metasurface-enabled multiplexing and Demultiplexing. *Adv. Mater.* **30**, e1800257 (2018).

27. J. Li, A. Díaz-Rubio, C. Shen, Z. Jia, S. Tretyakov, S. A. Cummer, Highly efficient generation of angular momentum with cylindrical bianisotropic metasurfaces. *Phys. Rev. Appl.* **11**, 024016 (2019).

28. S. Wang, G. Ma, C. T. Chan, Topological transport of sound mediated by spin-redirection geometric phase. *Sci. Adv.* **4**, eaaq1475 (2018).

29. F. Liu, W. Li, Z. Pu, M. Ke, Acoustic waves splitter employing orbital angular Momentum. *Appl. Phys. Lett.* **114**, 193501 (2019).

30. Y. Li, C. Shen, Y. Xie, J. Li, W. Wang, S. A. Cummer, Y. Jing, Tunable asymmetric transmission via lossy acoustic metasurfaces. *Phys. Rev. Lett.* **119**, 035501 (2017).

31. C. Shen, S. A. Cummer, Harnessing multiple internal reflections to design highly absorptive acoustic metasurfaces. *Phys. Rev. Appl.* **9**, 054009 (2018).

32. Y. Fu, C. Shen, Y. Cao, L. Gao, H. Chen, C. T. Chan, S. A. Cummer, Y. Xu, Reversal of transmission and reflection based on acoustic metagratings with integer parity design. *Nat. Commun.* **10**, 2326 (2019).

33. Y. Cao, Y. Fu, Q. Zhou, X. Ou, L. Gao, H. Chen, Y. Xu, Mechanism behind angularly asymmetric diffraction in phase-gradient metasurfaces. *Phys. Rev. Appl.* **12**, 024006 (2019).

34. Y. Xu, Y. Fu, H. Chen, Planar gradient metamaterials. *Nat. Rev. Mater.* **1**, 16067 (2016).

35. B. Assouar, B. Liang, Y. Wu, Y. Li, J.-C. Cheng, Y. Jing, Acoustic metasurfaces. *Nat. Rev. Mater.* **3**, 460–472 (2018).

36. X. Wang, X. Fang, D. Mao, Y. Jing, Y. Li, Extremely asymmetrical acoustic metasurface mirror at the exceptional point. *Phys. Rev. Lett.* **123**, 214302 (2019).

37. W. Wang, Y. Xie, B.-I. Popa, S. A. Cummer, Subwavelength diffractive acoustics and wavefront manipulation with a reflective acoustic metasurface. *J. Appl. Phys.* **120**, 195103 (2016).

38. Y. Xu, Y. Fu, H. Chen, Steering light by a sub-wavelength metallic grating from transformation optics. *Sci. Rep.* **5**, 12219 (2015).

39. Y. Xie, W. Wang, H. Chen, A. Konneker, B.-I. Popa, S. A. Cummer, Wavefront modulation and subwavelength diffractive acoustics with an acoustic metasurface. *Nat. Commun.* **5**, 5553 (2014).

40. Y. Li, S. Qi, M. B. Assouar, Theory of metascreen-based acoustic passive phased array. *New J. Phys.* **18**, 043024 (2016).

41. Y. Fu, Y. Cao, Y. Xu, Multifunctional reflection in acoustic metagratings with simplified design. *Appl. Phys. Lett.* **114**, 053502 (2019).

42. Y.-Y. Fu, J.-Q. Tao, A.-L. Song, Y.-W. Liu, Y.-D. Xu, Controllably asymmetric beam splitting via gap-induced diffraction channel transition in dual-layer binary metagratings. *Front. Phys.* **15**, 52502 (2020).

43. N. J. R. K. Gerard, Y. Li, Y. Jing, Investigation of acoustic metasurfaces with constituent material properties considered. *J. Appl. Phys.* **123**, 124905 (2018).

44. N. J. R. K. Gerard, H. Cui, C. Shen, Y. Xie, S. Cummer, X. Zheng, Y. Jing, Fabrication and experimental demonstration of a hybrid resonant acoustic gradient index metasurface at 40 kHz. *Appl. Phys. Lett.* **114**, 231902 (2019).

45. J. Li, C. Shen, A. Díaz-Rubio, S. Tretyakov, S. A. Cummer, Systematic design and experimental demonstration of bianisotropic metasurfaces for scattering-free manipulation of acoustic wavefronts. *Nat. Commun.* **9**, 1342 (2018).

Citation: Y. Fu, C. Shen, X. Zhu, J. Li, Y. Liu, S. A. Cummer, Y. Xu, Sound vortex diffraction via topological charge in phase gradient metagratings. *Sci. Adv.* **6**, eaba9876 (2020).